



A Mn-N₃ single-atom catalyst embedded in graphitic carbon nitride for efficient CO₂ electroreduction

Jiaqi Feng^{1,2,6}, Hongshuai Gao^{1,6}, Lirong Zheng³, Zhipeng Chen^{4,5}, Shaojuan Zeng¹, Chongyang Jiang^{1,2}, Haifeng Dong¹, Licheng Liu^{4,5}, Suojiang Zhang^{1,2}[✉] & Xiangping Zhang^{1,2,4}[✉]

Developing effective catalysts based on earth abundant elements is critical for CO₂ electroreduction. However, simultaneously achieving a high Faradaic efficiency (FE) and high current density of CO (j_{CO}) remains a challenge. Herein, we prepare a Mn single-atom catalyst (SAC) with a Mn-N₃ site embedded in graphitic carbon nitride. The prepared catalyst exhibits a 98.8% CO FE with a j_{CO} of 14.0 mA cm⁻² at a low overpotential of 0.44 V in aqueous electrolyte, outperforming all reported Mn SACs. Moreover, a higher j_{CO} of 29.7 mA cm⁻² is obtained in an ionic liquid electrolyte at 0.62 V overpotential. In situ X-ray absorption spectra and density functional theory calculations demonstrate that the remarkable performance of the catalyst is attributed to the Mn-N₃ site, which facilitates the formation of the key intermediate COOH* through a lowered free energy barrier.

¹Beijing Key Laboratory of Ionic Liquids Clean Process, State Key Laboratory of Multiphase Complex Systems, Institute of Process Engineering, Chinese Academy of Sciences, 100190 Beijing, P.R. China. ²College of Chemical Engineering, University of Chinese Academy of Science, 100049 Beijing, P.R. China. ³Beijing Synchrotron Radiation Facility (BSRF), Institute of High Energy Physics, Chinese Academy of Sciences, 100049 Beijing, P.R. China. ⁴Dalian National Laboratory for Clean Energy, 116023 Dalian, P.R. China. ⁵Qingdao Institute of Bioenergy and Bioprocess Technology, Chinese Academy of Sciences, 266101 Qingdao, P.R. China. ⁶These authors contributed equally: Jiaqi Feng, Hongshuai Gao. ✉email: sjzhang@ipe.ac.cn; xpzhang@ipe.ac.cn

Electrochemical CO₂ reduction reaction (CO₂RR) is one of the most promising ways to relieve CO₂ accumulation^{1,2}. Nevertheless, the CO₂RR process involves multiple proton–electron transfer reactions, and the H₂ evolution reaction (HER) always competes with it. Novel catalysts are strongly desirable to simultaneously obtain a high Faradaic efficiency (FE) and high current density of target products³. Among the various products of CO₂RR, CO is one of the most practical targets, since it can be used to prepare synthetic fuels and chemicals via a downstream Fischer–Tropsch process^{4–7}. Electrocatalysts based on manganese (Mn), the third most abundant transition metal in Earth's crust, have been reported as catalysts for the CO₂RR, including Mn oxides⁸, Mn complexes⁹, Mn single-atom catalysts (SACs)^{10–13}, and so on. Among them, Mn SACs have attracted great interest. However, the reported Mn SACs often use graphene as a substrate to form the Mn–N₄ structure, and the performance for CO₂RR is greatly limited, especially with regard to the CO partial current density (j_{CO}). Strasser et al. fabricated a family of SACs (M–N–C) with a variety of transition metals, including Mn–N–C which exhibited only 65% CO FE with a j_{CO} of 3.3 mA cm⁻²¹⁰. Zhang et al. reported a new Mn SAC with halogen and nitrogen dual coordination ((Cl, N)–Mn/G) and found that it is an efficient strategy to improve CO₂RR performance through controlling coordination of the active site by additional halogen in the SAC. The (Cl, N)–Mn/G showed a high CO FE of 97% at an overpotential of 0.49 V, while the j_{CO} was 9.2 mA cm⁻²¹¹. Therefore, it is significant to synthesize new Mn SACs with high j_{CO} and CO FE.

Herein, we prepare a Mn SAC with a Mn–N₃ site embedded in graphitic carbon nitride (g–C₃N₄) on carbon nanotubes (CNTs) for efficient CO₂RR, which is denoted as Mn–C₃N₄/CNT. The prepared catalyst displayed a 98.8% CO FE with a j_{CO} of 14.0 mA cm⁻² at a low overpotential of 0.44 V in aqueous electrolyte, which outperforms all Mn SACs reported in the literature. Interestingly, the j_{CO} was further improved in an ionic liquid (IL) electrolyte. In situ X-ray absorption spectra and density functional theory (DFT) calculations were conducted to investigate the process of CO₂ adsorption, activation and conversion over Mn–C₃N₄/CNT, demonstrating that three N atoms coordinated to a Mn center in g–C₃N₄ can greatly improve the performance of the Mn SAC in the CO₂RR. This work shows a means to enhance the CO₂RR performance of Mn-based catalysts under mild conditions.

Results

Synthesis and structural characterizations of Mn–C₃N₄/CNT. Mn–C₃N₄/CNT was synthesized through thermal pyrolysis of Mn acetate, CNTs, and dicyandiamide (DCD) under nitrogen at 873 K followed by hydrochloric acid washing, and the addition of CNTs served to improve the g–C₃N₄ conductivity. Scanning electron microscopy (SEM) and transmission electron microscopy (TEM) images show that Mn–C₃N₄/CNT maintains the morphology of the CNTs without the formation of obvious particles (Fig. 1a, b). A thin enveloping layer of g–C₃N₄ (confirmed by powder X-ray diffraction (XRD) and X-ray photoelectron spectroscopy (XPS)) is observed on the surface of CNTs at a higher magnification (Fig. 1c). Energy-dispersive X-ray spectroscopy (EDS) images reveal that Mn, N, and C are homogeneously distributed on the entire surface of Mn–C₃N₄/CNT (Fig. 1d). For comparison, C₃N₄/CNT and Mn/CNT were synthesized by the same procedure as Mn–C₃N₄/CNT except for the omission of Mn acetate and DCD, respectively. It is worth pointing out that Mn/CNT was not treated by acid washing, as Mn was removed after acid washing, leading to inactivation of the catalyst. The morphologies of C₃N₄/CNT and Mn/CNT are

almost identical except that there are obvious particles on Mn/CNT (Supplementary Figs. 1–3). The main peaks in the XRD pattern of Mn/CNT can be indexed as the Mn₃O₄ phase (JCPDS Card No. 75-1560), indicating the formation of a Mn₃O₄/CNT composite (Fig. 1e). For Mn–C₃N₄/CNT and C₃N₄/CNT, peaks at 25.8° and 42.8° can be ascribed to the (002) and (100) facets of the CNTs¹⁴, respectively, and no peak of g–C₃N₄ is observed. However, a peak appears at 27.4° after the amount of DCD is increased (Supplementary Fig. 4), which can be indexed to the interplanar stacking of aromatic systems of g–C₃N₄¹⁵. Therefore, the absence of g–C₃N₄ peaks in the Mn–C₃N₄/CNT XRD pattern is because they are covered by the high-intensity CNT peaks. Meanwhile, the absence of metallic peaks indicates that there are no crystalline metal-containing phases or clusters, which is in good agreement with the TEM results. The aberration-corrected HAADF-STEM image confirms the existence of atomically dispersed Mn in Mn–C₃N₄/CNT (Fig. 1f), and the Mn content is 0.17 wt% as measured by inductively coupled plasma atomic emission spectroscopy. The contents of N and C detected by elemental analysis are 9.8 and 81.1 wt%, respectively. Moreover, the specific surface areas of C₃N₄/CNT (271 cm² g⁻¹) and Mn–C₃N₄/CNT (221 cm² g⁻¹) are larger than that of Mn₃O₄/CNT (188 cm² g⁻¹), indicating that the thin enveloping layer of g–C₃N₄ on the surface of CNTs can increase the specific surface area (Supplementary Fig. 5).

Fine structure of Mn–C₃N₄/CNT. The chemical composition and elemental state of Mn–C₃N₄/CNT, C₃N₄/CNT, and Mn₃O₄/CNT were examined by XPS. The full XPS survey of Mn–C₃N₄/CNT scan shows the presence of Mn, N, C, and O (Supplementary Fig. 6). The existence of O is attributed to C=O or C–O groups on the surface of CNTs. The high-resolution XPS N 1s spectrum of Mn–C₃N₄/CNT (Fig. 2a) can be divided into triazine rings (C–N–C, ~398.9 eV, 33.6%), Mn–N (~399.8 eV, 17.0%), tertiary nitrogen (N–(C)₃, ~400.4 eV, 38.6%), and amino functions (N–H, ~401.6 eV, 10.8%) of g–C₃N₄¹⁶. Compared with that of the N 1s spectrum of C₃N₄/CNT (Fig. 2b), the percentage of Mn–N increases from 0% to 17.0%, and the percentage of C–N–C decreases by ~15.4%, suggesting that C–N–C is most likely to provide coordination sites for Mn atoms to form Mn–N_x moieties. The XPS Mn 2p spectra of Mn–C₃N₄/CNT and Mn₃O₄/CNT are displayed in Supplementary Fig. 7, and the Mn 2p_{3/2} spectrum of Mn₃O₄/CNT is divided into two kinds of valence states, located at 641.2 and 642.9 eV, ascribed to Mn²⁺ and Mn³⁺, respectively¹⁷. The Mn 2p_{3/2} peak of Mn–C₃N₄/CNT is close to Mn²⁺, suggesting that the valence state of the Mn atom in Mn–C₃N₄/CNT is likely to be +2. The local structure of the catalyst at the atomic level was further determined by X-ray absorption spectroscopy (XAS). For the Mn K-edge X-ray absorption near-edge structure (XANES, Fig. 2c), the absorption edge of Mn–C₃N₄/CNT is close to that of MnO, located between Mn foil and Mn₃O₄, which further suggests that the valence state of Mn in Mn–C₃N₄/CNT is close to +2. The formation of Mn–N bonds in Mn–C₃N₄/CNT is directly confirmed by the phase-uncorrected Fourier transformed (FT) extended X-ray absorption fine structure (EXAFS) characterization (Fig. 2d). Mn foil presents the main peak at 2.3 Å, corresponding to the scattering path of Mn–Mn^{16,18}. For Mn–C₃N₄/CNT, no Mn–Mn bond peak is detected, indicating atomically dispersed Mn. For the EXAFS spectrum of Mn–C₃N₄/CNT, the peak at 1.7 Å can be ascribed to Mn–N or Mn–O. For the XAS spectrum of the O K-edge, the Mn–O peak is not detected, and no difference in position between Mn–C₃N₄/CNT and C₃N₄/CNT (Fig. 2e) is found. Further considering the XPS results that the N atom of C–N–C provides a coordination site to form the Mn–N structure, the peak at 1.7 Å is

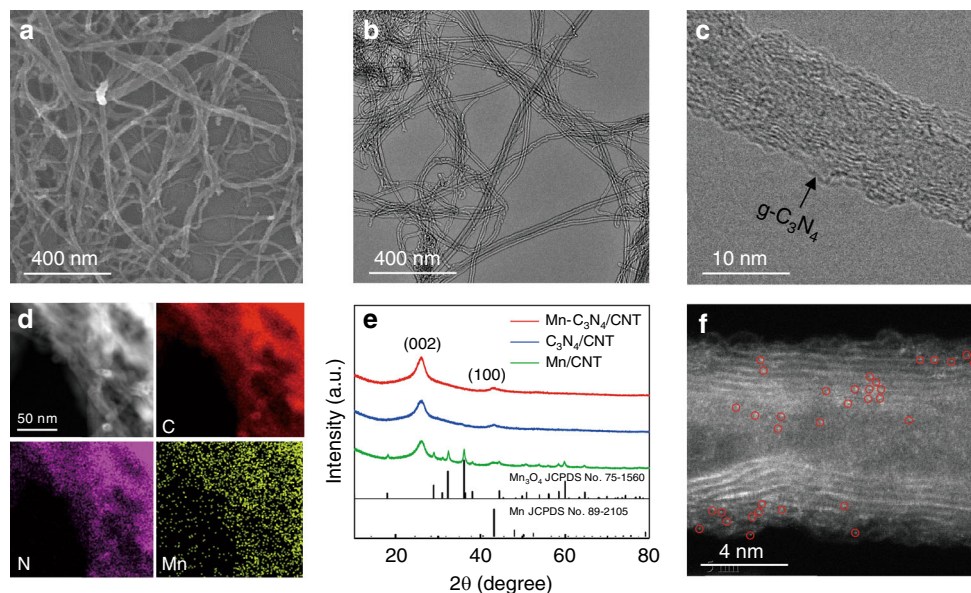


Fig. 1 Structural characterizations of Mn-C₃N₄/CNT. **a** SEM image of Mn-C₃N₄/CNT. **b** Large-field view and **c** magnified view of TEM images of Mn-C₃N₄/CNT. **d** EDS mapping of Mn-C₃N₄/CNT. **e** XRD patterns of Mn-C₃N₄/CNT, C₃N₄/CNT, and Mn/CNT. **f** HAADF-STEM image of Mn-C₃N₄/CNT with the atomic dispersion of Mn highlighted by red circles.

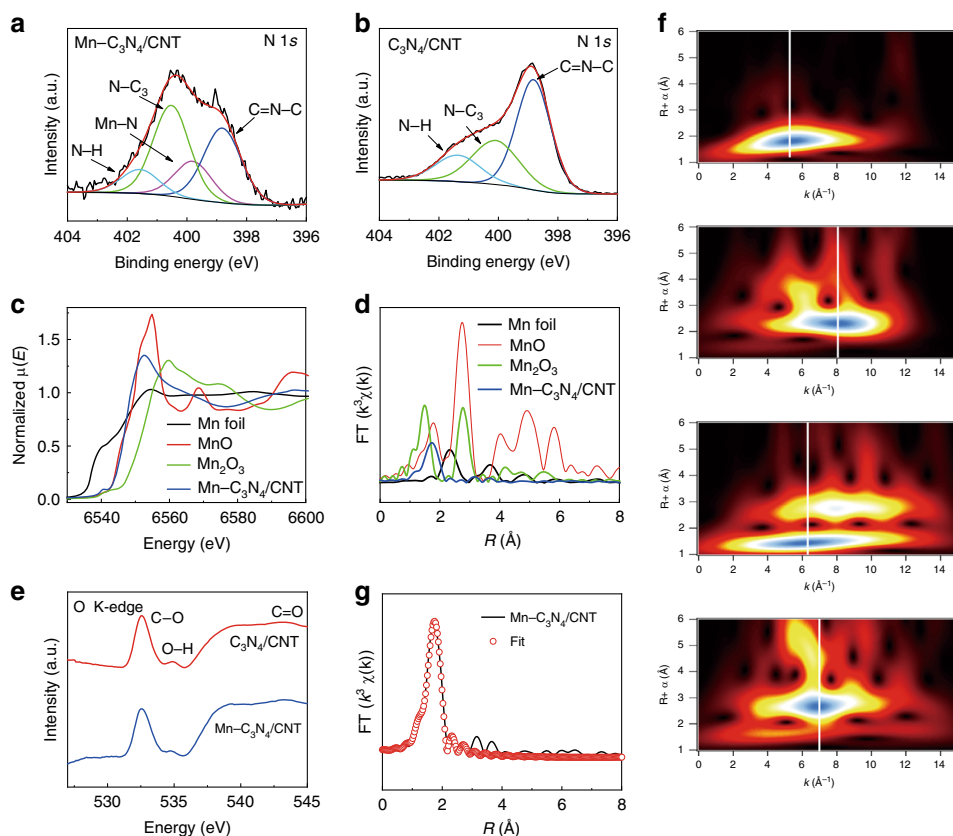


Fig. 2 Fine structure of Mn-C₃N₄/CNT. **a, b** High-resolution N 1s XPS spectra of Mn-C₃N₄/CNT and C₃N₄/CNT, respectively. **c, d** XANES and EXAFS spectra at the Mn K-edge. **e** O K-edge XAS of Mn-C₃N₄/CNT and C₃N₄/CNT. **f** WT of Mn-C₃N₄/CNT, Mn foil, Mn₂O₃, and MnO (from top to bottom). **g** EXAFS fitting curves of Mn-C₃N₄/CNT in R space.

ascribed to the scattering path of Mn-N¹⁸. The wavelet transform (WT) results further verify that Mn-Mn bonds are not present in Mn-C₃N₄/CNT, and the peak of Mn-C₃N₄/CNT tends to have a lower k value than that of Mn-O in Mn₂O₃ and MnO, indicating that the Mn-N bond is more likely to exist in Mn-C₃N₄/CNT

(Fig. 2f). Quantitative EXAFS curve fitting analysis (Fig. 2g and Supplementary Table 1) was performed to investigate the structural parameters of Mn-C₃N₄/CNT, and the best-fitting analysis clearly confirms that the Mn-N coordination number is ~3.2, meaning that the isolated Mn atom is threefold coordinated by

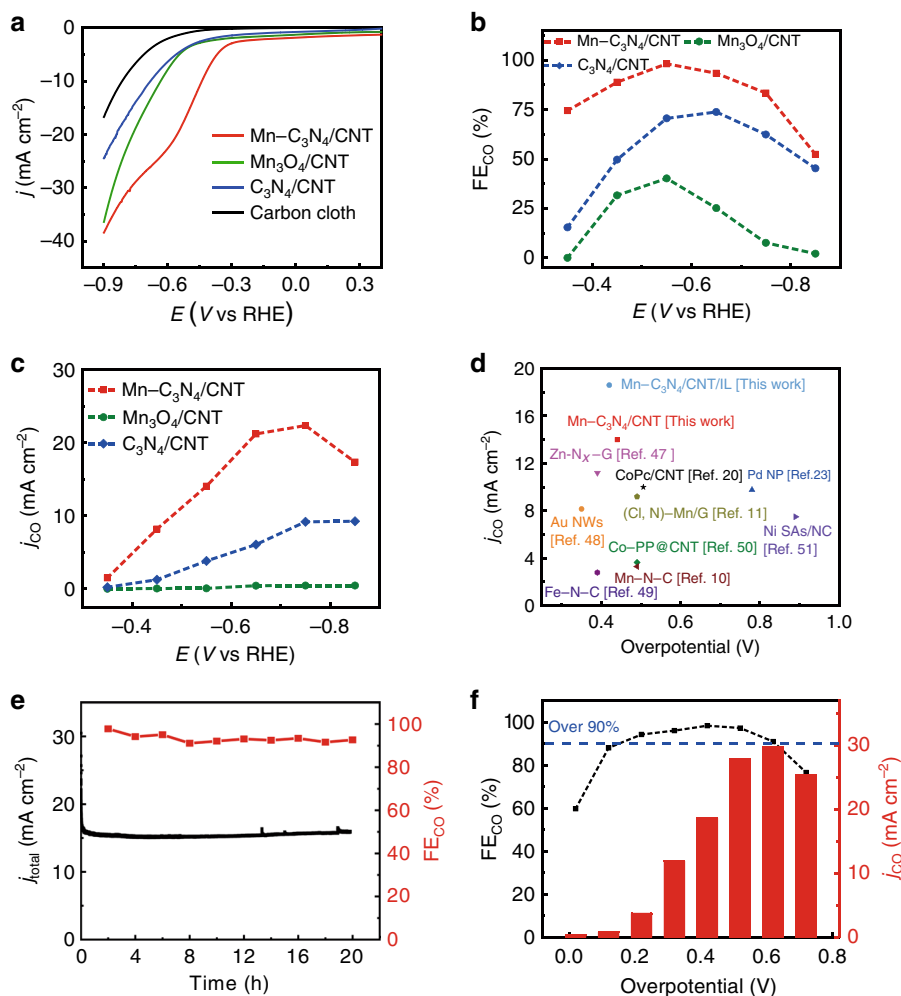


Fig. 3 The CO₂RR performance over Mn-C₃N₄/CNT, C₃N₄/CNT, and Mn₃O₄/CNT. **a** LSV curves in the CO₂-saturated KHCO₃ electrolyte (pH: 7.33, temperature: 25 ± 3 °C, without stirring). **b** FE_{CO} and **c** *j*_{CO} at different applied potentials. **d** *j*_{CO} of Mn-C₃N₄/CNT at the maximum CO FE compared with those of most state-of-the-art catalysts^{10,11,20,23,47–51}. **e** Long-term durability of Mn-C₃N₄/CNT operated at –0.55 V for 20 h. **f** FE_{CO} and *j*_{CO} of Mn-C₃N₄/CNT at different applied potentials in the CO₂-saturated [Bmim]BF₄/CH₃CN-H₂O electrolyte.

N atoms. The calculated Mn–N mean bond distance in Mn–C₃N₄/CNT is 2.21 Å which is longer than that of the Mn–N₄ (2.02 Å) structure¹¹. The results of the best-fitting analysis demonstrate that the coordination environment of the Mn atom in Mn–C₃N₄/CNT is different from that of Mn SACs reported in the literature^{10,12,13}, which may cause different CO₂RR performance.

Electrochemical activities of CO₂ reduction. Inspired by the Mn–N₃ site in Mn–C₃N₄/CNT, its CO₂RR performance was evaluated in a CO₂-saturated 0.5 M KHCO₃ electrolyte by linear sweep voltammetry (LSV). For comparison, C₃N₄/CNT, Mn₃O₄/CNT and carbon cloth were also measured. Mn–C₃N₄/CNT exhibits a more positive onset potential and higher current density than those of other catalysts (Fig. 3a). A cathodic peak appears at approximately –0.5 V (vs. the reversible hydrogen electrode (vs. RHE)); all potentials are referenced to RHE) in the LSV curve of Mn–C₃N₄/CNT, and the peak current increases linearly with scan rate (Supplementary Fig. 8), which indicates that the peak originates from the CO₂ mass transfer-controlled electrolysis process^{11,19}. Furthermore, the LSV curve of Mn–C₃N₄/CNT exhibits the absence of the cathodic peak and the low current density in the N₂-saturated electrolyte (Supplementary Fig. 9), suggesting its high CO₂RR activity. The electrolysis

tests were performed in an H-type cell to evaluate the selectivity of different catalysts for CO₂RR. CO and H₂ were the only gas products in the gas phase and no liquid product was detected. Mn–C₃N₄/CNT shows outstanding performance (Fig. 3b), and the CO FE reaches a maximum of 98.8% at –0.55 V, while C₃N₄/CNT and Mn₃O₄/CNT only show maximum CO FE of 70.6% and 40.2%, respectively. The H₂ FE of Mn–C₃N₄/CNT is much lower than that of C₃N₄/CNT and Mn₃O₄/CNT at all applied potentials (Supplementary Fig. 10). Combining the total current density and the corresponding CO FE, *j*_{CO} was obtained under different applied potentials. Mn–C₃N₄/CNT exhibits a *j*_{CO} of 14.0 mA cm^{–2} at –0.55 V and the highest *j*_{CO} of 22.4 mA cm^{–2} is obtained at –0.75 V (Fig. 3c); these values are much higher than those of C₃N₄/CNT and Mn₃O₄/CNT (<5 mA cm^{–2}). Comparing the performance of various catalysts reported in the literature, it can be concluded that Mn–C₃N₄/CNT outperforms all reported Mn SACs and is one of the best reported electrocatalysts for CO₂ conversion to CO (Fig. 3d, Supplementary Table 2)^{20–23}. To further verify the important role of Mn–N₃ in the reaction, we adopted the method reported in the literature to destroy the structure through an annealing process at 1273 K in a N₂ atmosphere (with the product denoted as Mn–NC/CNT)^{24,25}. Both the CO FE and *j*_{CO} of Mn–NC/CNT decrease evidently compared with those of Mn–C₃N₄/CNT (Supplementary Fig. 11), confirming the active

site role of Mn-N₃. To test the stability of the catalyst, a 20 h electrolysis experiment was performed on Mn-C₃N₄/CNT, and the CO FE and current density did not obviously decay (Fig. 3e). Additionally, no noticeable change can be observed in the morphology of Mn-C₃N₄/CNT, and the atomic contents of C-N-C (29.9%), Mn-N (17.5%), N-(C)₃ (39.8%), and N-H (12.7%) fall into the statistical region of the atomic content of N moieties for pristine Mn-C₃N₄/CNT after long-term electrolysis (Supplementary Fig. 12). All of these results indicate the excellent stability of Mn-C₃N₄/CNT for the CO₂RR. A large electrochemical active surface area (ECSA) can contribute to the activity of catalyst. The measured double-layer capacitance of catalysts is displayed in Supplementary Figs. 13 and 14, in which the slope could be a reference for the ECSA. Mn-C₃N₄/CNT and C₃N₄/CNT share a similar ECSA, which is much larger than that of Mn₃O₄/CNT, suggesting that the g-C₃N₄ enveloped on the CNT's surface can increase the ECSA, but it is not the key reason for the final performance of Mn-C₃N₄/CNT. Nyquist plots were obtained at the open-circuit potential to investigate kinetic reactions on the electrode/electrolyte interface (Supplementary Fig. 15) and the data were fitted using a simple equivalent circuit R(CR)W. The results show that Mn-C₃N₄/CNT undergoes a faster interfacial charge-transfer process during the CO₂ reaction process than the other catalysts, which could improve the reaction activity.

Compared with aqueous electrolytes, IL electrolytes have many unique physicochemical properties, such as a wide electrochemical potential window, large absorption capacity of CO₂, and high intrinsic ionic conductivity, which are beneficial to the CO₂RR^{26–28}. Therefore, the activity of Mn-C₃N₄/CNT was tested in a CO₂-saturated IL electrolyte (1-butyl-3-methylimidazolium tetrafluoroborate ([Bmim][BF₄])/acetonitrile (CH₃CN)-H₂O)^{29,30}. Since the reference electrode (Ag/Ag⁺ electrode) used for the organic electrolyte is different from that (Ag/AgCl electrode) for aqueous electrolyte and the equilibrium potential for CO is -1.68 V vs. Ag/Ag⁺ in the IL electrolyte (Supplementary Fig. 16)^{31,32}, the overpotential is adopted for the following discussion. Figure 3f shows that the CO FE of Mn-C₃N₄/CNT maintains over 90% in a wide overpotential range from 0.22 to 0.62 V and reaches a maximum of 98.3% at 0.42 V overpotential. Meanwhile, Mn-C₃N₄/CNT exhibits a *j*_{CO} of 18.6 mA cm⁻² at the maximum CO FE. The highest *j*_{CO} value of 29.7 mA cm⁻² is obtained at an overpotential of 0.62 V, which is higher than that of Mn-C₃N₄/CNT in the KHCO₃ electrolyte. ¹³CO₂ was also used as the feedstock to carry out the electrolysis test in the IL electrolyte and it was confirmed that CO is the conversion product of CO₂ (Supplementary Fig. 17). The enhanced performance of Mn-C₃N₄/CNT in the IL electrolyte is probably based on the following mechanism. First, the CO₂ solubility of [Bmim][BF₄] is much higher than that in aqueous solution, which alleviates the resistance of mass transfer on the CO₂RR³³. Second, it has been reported that the imidazolium cation of IL can electrostatically be arranged at the cathode to favor CO₂ adsorption via [Bmim-CO₂]⁺, which could help to lower the activation energy for the CO₂ reduction process^{27,34}. Therefore, it is an efficient strategy to enhance the performance of catalysts by integration with an IL electrolyte, especially in terms of the current density and the overpotential.

Discussion

The results mentioned above demonstrate that Mn-C₃N₄/CNT has excellent CO₂RR activity. Therefore, in situ XAS analysis and DFT calculations were performed to shed light on the process of CO₂ reduction over Mn-C₃N₄/CNT. The Mn K-edge XANES and EXAFS spectra of Mn-C₃N₄/CNT were recorded under in situ conditions. As shown by the XANES spectra (Fig. 4a), the Mn K-edge of Mn-C₃N₄/CNT increased by 0.15 eV in the

CO₂-saturated electrolyte under the open-circuit voltage compared with that in the N₂-saturated electrolyte. This result could be attributed to the increase in the Mn oxidation state owing to the redistribution of electrons after CO₂ adsorption on the Mn site, transferring from the Mn site to the carbon 2*p* orbital in CO₂ to form a CO₂^{•-} species³⁵. When a potential of -0.55 V was applied on the electrode in the CO₂-saturated electrolyte, a CO₂ electroreduction reaction occurred, and the Mn K-edge of Mn-C₃N₄/CNT shifted back to lower energy, which suggests that the Mn valence state returns to the low valence state after one cycle of CO₂ reduction³⁶. In the FT EXAFS spectra (Fig. 4b), the intensity of the main peak at ~1.7 Å increased slightly in the CO₂-saturated electrolyte compared with that in the N₂-saturated electrolyte, which can be attributed to the formation of a C-Mn³⁷ bond when the Mn site interacted with CO₂. The main peak shifted to a longer length (~1.76 Å) when applying voltage to the electrode, indicating the lengthening of the Mn-N bond due to the redistribution of electrons among Mn, N, and C (from adsorbed CO₂). The results from the in situ XAS spectra indicate that the Mn-N₃ site in Mn-C₃N₄/CNT is the active site for the CO₂RR, on which CO₂ is adsorbed, activated, and converted.

The coordination number of Mn in Mn-C₃N₄/CNT is 3.2, which is slightly different from that of the Mn-N₃ moiety. In general, it is accepted by researchers to use the integral value of the best-fitted coordination number to represent the structure of the catalyst active site in DFT calculations^{38,39}, because there is an error bound while using the data from EXAFS to fit the coordination number. Therefore, a coordination number of three (Mn-N₃) is adopted as the catalyst structure for building a DFT model. The catalyst structure is optimized according to the literature¹⁸, which indicated that a single atom of Mn interacting with the edge of g-C₃N₄ is the optimal structure. On this basis, the structure of the catalyst is further optimized and the results indicate that the Mn atom interacting with the edge of g-C₃N₄ via three bonds (Mn-N₃-C₃N₄) is most stable. Moreover, the coordination number and the average Mn-N bond length (2.11 Å) of Mn-N₃-C₃N₄ are basically consistent with the EXAFS results. Therefore, Mn-N₃-C₃N₄ is confirmed as the structure of Mn-C₃N₄/CNT, which is obviously different from that of reported Mn SACs (Mn-N₄ moiety embedded in graphene, Mn-N₄-G)^{10,13} (Supplementary Figs. 18 and 19, Supplementary Table 3, and Supplementary Note 1). The positions of the *d*-band centers of Mn-N₃-C₃N₄ and Mn-N₄-G were calculated to investigate their electronic structures. Figure 4c shows that the position of the *d*-band center for Mn-N₃-C₃N₄ is closer to the Fermi level than that of Mn-N₄-G, indicating Mn-N₃-C₃N₄ is more favorable to the binding and activation of CO₂. The above results suggest that the electronic structures of Mn-N₃-C₃N₄ and Mn-N₄-G are different, which may lead to different catalytic mechanisms. Thus, DFT calculations were performed to investigate the mechanisms of CO₂RR. The CO₂ electroreduction to CO involves two electrons and two protons: (I) CO₂ + * + H⁺ + e⁻ → *COOH; (II) *COOH + H⁺ + e⁻ → *CO + H₂O; and (III) *CO → CO + * (* represents the active site of catalyst). The structures of the COOH* and CO* reaction intermediates on the catalysts are displayed in Supplementary Figs. 20 and 21, it can be seen that the Mn atoms in Mn-N₃-C₃N₄ are distorted out of the g-C₃N₄ plane, and the average Mn-N bond length (2.18 Å) is longer than that of the original Mn-N₃-C₃N₄ (2.11 Å) after interacting with COOH*, which is in accordance with the in situ XAS spectral results. Moreover, Mn-N₃-C₃N₄ presents a higher adsorption energy of COOH* ($\Delta E_{\text{ads}} = -1.998$ eV) than Mn-N₄-G ($\Delta E_{\text{ads}} = -1.367$ eV), indicating that COOH* is more stable on Mn-N₃-C₃N₄ than Mn-N₄-G (Supplementary Table 4). The free energy profiles of CO₂ electroreduction to CO are shown in Fig. 4d. The potential-determining steps of

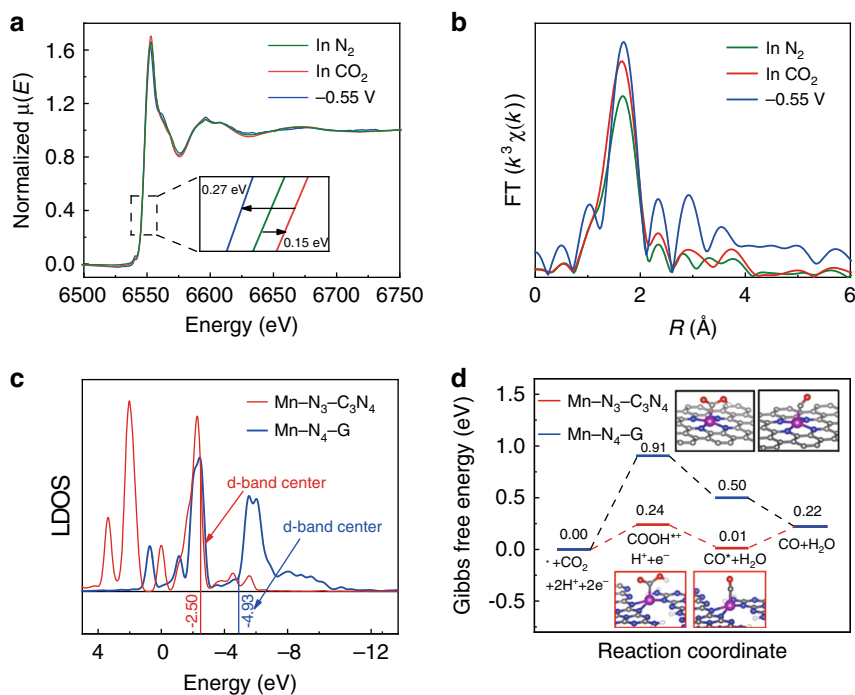


Fig. 4 In situ XAS experiments and DFT calculations. **a, b** XANES and EXAFS spectra at the Mn K-edge of Mn-C₃N₄/CNT under various conditions. **c** Local density of states (LDOS) of Mn in Mn-N₃-C₃N₄ and Mn-N₄-G. **d** Calculated Gibbs free energy diagrams for CO₂RR over Mn-N₃-C₃N₄ and Mn-N₄-G.

Mn-N₃-C₃N₄ and Mn-N₄-G are both the first-step reduction of CO₂ to form the COOH* intermediate, corresponding to free energy increases of 0.24 and 0.91 eV, respectively. Clearly, Mn-N₃-C₃N₄ has much a lower Gibbs free energy for COOH* formation. The results of the DFT calculations confirm that Mn-N₃-C₃N₄ is an efficient site for CO₂ conversion.

In summary, we fabricated a Mn SAC with a Mn-N₃ active site and applied it to the CO₂RR. The synthesized Mn SAC exhibited a 98.8% CO FE with a high j_{CO} of 14 mA cm⁻² at an overpotential of 0.44 V in aqueous electrolyte. When an IL is used as the electrolyte, higher j_{CO} of 18.6 and 29.7 mA cm⁻² are obtained at an overpotential of 0.42 and 0.62 V, respectively. In situ XAS spectra and DFT calculations indicate that the Mn-N₃ site is the active center, on which CO₂ is more easily adsorbed and the free energy barrier of key intermediate formation is greatly decreased. It can be anticipated that Mn SACs may also exhibit excellent performance in other electrochemical reactions by changing the supporting materials to form exclusive active sites.

Methods

Materials. Manganous acetate (Mn(COOH)₂·4H₂O) (99.99%) and DCD (>98%) were purchased from Shanghai Aladdin Biochemical Tech. Co., Ltd. Multiwalled carbon nanotubes (MWCNTs) were provided by XFNANO. Carbon cloth (HCP331P, 19 × 19 cm), Nafion D-521 dispersion (5% w/w in water and 1-propanol, ≥0.92 meq/g exchange capacity), and Nafion N-117 membrane (0.180 mm thick, ≥0.90 meq/g exchange capacity) were purchased from Shanghai Hesen Electric Co., Ltd. 1-butyl-3-methylimidazolium tetrafluoroborate ([Bmim]BF₄, purity >99%) was purchased from Shanghai Chengjie Co., Ltd. The IL was purified and dried before use. Sulfuric acid (AR grade) was purchased from Beijing Chemical Company. All aqueous solutions were prepared with Milli-Q water.

Surface modification of MWCNTs. Hydrophilic functional groups were produced on the surface of the MWCNTs by oxidation treatment. First, 200 mg of pristine MWCNTs was dispersed in 50 mL of mixed acid (3:1 v/v solution of sulfuric acid and nitric acid) with the assistance of sonication and then stirred at room temperature for 24 h. After repeatedly washing with water, the treated MWCNTs were stirred with 25 mL of 5 M nitric acid at room temperature for 24 h to remove metal impurities, sequentially washed with water and finally vacuum dried.

Synthesis of Mn-C₃N₄/CNT. First, 25 mg of treated MWCNTs, 50 mg of DCD and 24 mg of Mn(COOH)₂·4H₂O were sonicated in 100 mL of water and then stirred at 323 K for 10 h. The mixture was dried using lyophilization and annealed at 873 K for 1 h under a nitrogen atmosphere. To obtain the final product of Mn-C₃N₄/CNT, the as-annealed powders were further washed with 1 M HCl followed by water and finally were subjected to vacuum drying.

Synthesis of Mn₃O₄/CNT and C₃N₄/CNT. Mn₃O₄ supported on CNTs was prepared by the same procedure as Mn-C₃N₄/CNT except for the omissions of DCD and HCl treatment. C₃N₄/CNT was prepared by the same procedure as Mn-C₃N₄/CNT except for the omission of metal salt.

Synthesis of Mn-C₃N₄ and pure g-C₃N₄. Mn-C₃N₄ was synthesized by the same procedure as Mn-C₃N₄/CNT except for the omission of MWCNTs. Pure g-C₃N₄ was prepared by the same procedure as Mn-C₃N₄/CNT except for the omissions of MWCNTs and metal salt.

Physical and chemical characterizations. Powder XRD measurements were recorded with a Rigaku Smartlab diffractometer with Cu Kα radiation ($\lambda = 1.5418 \text{ \AA}$) operated at 45 kV and an emission of 50 mA. The scattering range of 2θ was from 5° to 90°, with a scanning rate of 15 min⁻¹. SEM was performed using a Hitachi SU8020 electron microscopy operated at 5 kV. TEM was performed on a JEOL JEM-2100 system. High-angle annular dark-field scanning transmission electron microscopy (HAADF-STEM) characterization and corresponding energy-dispersive spectroscopy (EDS) were conducted on a JEOL JEM-ARF200F TEM/STEM system with a spherical aberration corrector. XPS was performed by a Thermo Fisher Scientific ESCALAB 250Xi using an Al Kα (1486.6 eV) X-ray source under a pressure of 3×10^{-7} mbar, and the binding energy was referenced to the C 1s peak at 284.8 eV. The N₂ adsorption-desorption isotherms of catalysts were recorded at 77 K on a Quantachrome Instrument NOVA 2000, and the specific surface area and pore size distribution were determined by the Brunauer-Emmett-Teller (BET) method and Barrett-Joyner-Halenda (BJH) model, respectively. The X-ray absorption fine structure spectra were collected at the 1W1B station in the Beijing Synchrotron Radiation Facility (BSRF). The storage rings of the BSRF were operated at 2.5 GeV with an average current of 250 mA. Using a Si (111) double-crystal monochromator, the data collection was carried out in fluorescence mode using an ionization chamber. All spectra were collected under ambient conditions, and XAFS data were processed according to standard procedures using the ATHENA module implemented in the IFFFIT software packages. The k^3 -weighted EXAFS spectra were obtained by subtracting the post-edge background from the overall absorption and then normalized with respect to the edge-jump step. Subsequently, the k^3 -weighted $\chi(k)$ data of the Mn K-edge were FT to real (R) space using hanging

windows ($dk = 1.0 \text{ \AA}^{-1}$) to separate the EXAFS contributions from different coordination shells. To obtain the quantitative structural parameters around central atoms, least-squares curve parameter fitting was performed using the ARTEMIS module of IFEFFIT software packages^{40–42}.

Electrochemical test. Fabrication of the working electrode: 1.0 mg of the catalyst was suspended in 240 μL of isopropanol and 40 μL of Nafion D-521 with ultrasound assistance to form a homogeneous ink. Then, the ink was dropped onto a carbon cloth ($1 \times 1 \text{ cm}^2$) surface by a micropipette and finally dried at room temperature. CO_2RR was conducted in a typical H-type electrochemical cell separated by a Nafion 117 membrane with a three-electrode system. A Ag/AgCl or Ag/Ag⁺ electrode and platinum gauze were used as the reference electrode and counter electrode, respectively. The working and reference electrodes were placed in the cathode chamber with a 0.5 M KHCO_3 solution or [Bmim][BF₄]/CH₃CN–H₂O mixture solution containing 30 wt% [Bmim][BF₄], 65 wt% CH₃CN, and 5 wt% H₂O as the electrolyte, while the counter electrode was placed in the anode chamber with a 0.1 M H₂SO₄ solution as the electrolyte. Before the experiment, the electrolyte in the cathode chamber was bubbled with N₂ or CO₂ (30 mL min^{−1}) for at least 30 min to form the N₂-saturated or CO₂-saturated solution, respectively, and magnetic stirring (240 r min^{−1}) was applied to the electrolyte during the experiment for better mixing. LSV measurements were recorded at a scan rate of 20 mV s^{−1}. ECSA referred to the cyclic voltammogram results under the potential windows of 0.5 V ~ 0.6 V with different scan rates of 5, 10, 20, 40 and 60 mV s^{−1}. For the FE analysis, the gas products were collected into a sampling bag. After electrolysis for 1 h, the products were analyzed and quantified by a gas chromatography (GC, Agilent 6820) system equipped with a thermal conductivity detector (TCD) and a flame ionization detector (FID) using nitrogen as the carrier gas. ¹H nuclear magnetic resonance (NMR) spectroscopy (Bruker Advance III HD 600) was employed to confirm and quantify the liquid products with phenol as an internal standard in DMSO-d₆. The quantification of gas and liquid products was determined by comparison with the standard curves. On the basis of GC and ¹H NMR analysis, the respective current density and FE of the products were calculated. The CO FE were calculated by the following formula:

$$\text{FE} = \frac{nF}{Q} \times 100 \quad (1)$$

where n represents the number of electrons transferred for product formation, which is 2 for CO, n is the total moles number of CO measured by GC, F is the Faraday constant (96,485 C mol^{−1}) and Q is the amount of cumulative charge recorded by the electrochemical workstation.

In situ XAS. A homemade electrochemical cell was employed for in situ XAS experiments under the sensitive fluorescence model. The cell was filled with the electrolyte, and a Ag/AgCl electrode and platinum gauze were used as the reference electrode and counter electrode, respectively. There is a single circular hole of 1.0 cm in diameter on the wall of the cell. The working electrode contacted with a slip of copper tape was placed to the exterior of the wall to cover the hole and Kapton (polyimide) tape was used to seal the cell. In situ XAS spectra were obtained at the open-circuit potential in N₂ or CO₂-saturated electrolyte and an applied potential of −0.55 V in the CO₂-saturated electrolyte.

Computational details for calculations. We carried out first-principle DFT calculations on the CO₂RR activity of Mn–N₃–C₃N₄ and Mn–N₄–G by the projector-augmented wave (PAW) method-based Vienna ab initio simulation package (VASP)^{43,44}. The functional of Perdew, Burke, and Ernzerhof (PBE) with generalized gradient approximation (GGA) was considered for the electron exchange-correlation⁴⁵. The cutoff energy for the plane-wave basis set was set as 450 eV. The vacuum layer was set to be more than 12 \AA to preclude coupling between periodic supercells. A Monkhorst–Pack k -point mesh of $5 \times 5 \times 1$ grid was used to sample the Brillouin zone. The convergence criteria were set to be $<10^{-5}$ eV in total energy and 0.01 eV \AA^{-1} in force. The adsorption energy of the COOH* and CO* intermediates were defined as the energy difference between the adsorbed complex and the sum of isolated Mn–N₃–C₃N₄/Mn–N₄–G catalyst and the isolated COOH* (CO*) group. For the electroreduction process, the model of a computational hydrogen electrode was used to calculate the energy of the proton–electron pair⁴⁶. The Gibbs free energy (ΔG) for each reaction process is calculated with the following equation:

$$\Delta G = \Delta E + \Delta E_{\text{ZPE}} - T\Delta S \quad (2)$$

where ΔE , ΔE_{ZPE} and ΔS , denote the changes in the DFT electronic energy, the zero-point energy, and the entropy at 300 K, respectively. For the vibrational entropy calculations, only the adsorbed species were allowed to move, while the catalytic substrate such as Mn–N₃–C₃N₄ or Mn–N₄–G was fixed.

Data availability

The data supporting the findings of this study are available within the article and its Supplementary information files. All data is available from the authors upon reasonable request.

Code availability

All code supporting the findings of this study are available from the corresponding author on request.

Received: 27 March 2020; Accepted: 5 August 2020;

Published online: 28 August 2020

References

- Turner, J. A. A realizable renewable energy future. *Science* **285**, 687–689 (1999).
- Gao, S. et al. Partially oxidized atomic cobalt layers for carbon dioxide electroreduction to liquid fuel. *Nature* **529**, 68–71 (2016).
- Bai, X. et al. Exclusive formation of formic acid from CO₂ electroreduction by a tunable Pd–Sn Alloy. *Angew. Chem. Int. Ed.* **56**, 12219–12223 (2017).
- Guo, S. et al. A Co₂O₄–CDots–C₃N₄ three component electrocatalyst design concept for efficient and tunable CO₂ reduction to syngas. *Nat. Commun.* **8**, 1828 (2017).
- Lee, J. H. et al. Tuning the activity and selectivity of electroreduction of CO₂ to synthesis gas using bimetallic catalysts. *Nat. Commun.* **10**, 3724 (2019).
- David, M. K. et al. Understanding the origin of highly selective CO₂ electroreduction to CO on Ni, N-doped carbon catalysts. *Angew. Chem. Int. Ed.* **59**, 4043–4050 (2020).
- Gao, F.-Y. et al. High-curvature transition metal chalcogenide nanostructures with profound proximity effect enable fast and selective CO₂ electroreduction. *Angew. Chem. Int. Ed.* **59**, 8706–8712 (2020).
- Peng, X. et al. Efficient electroreduction CO₂ to CO over MnO₂ nanosheets. *Inorg. Chem.* **58**, 8910–8914 (2019).
- Myren, T. H. T. et al. Metalloradical intermediates in electrocatalytic reduction of CO₂ to CO: Mn versus Re bis-N-heterocyclic carbene pincers. *Dalton Trans.* **49**, 2053–2057 (2020).
- Varela, A. S. et al. Metal-doped nitrogenated carbon as an efficient catalyst for direct CO₂ electroreduction to CO and hydrocarbons. *Angew. Chem. Int. Ed.* **54**, 10758–10762 (2015).
- Zhang, B. et al. Manganese acting as a high-performance heterogeneous electrocatalyst in carbon dioxide reduction. *Nat. Commun.* **10**, 2980 (2019).
- Pan, F., Deng, W., Justiniano, C. & Li, Y. Identification of champion transition metals centers in metal and nitrogen-codoped carbon catalysts for CO₂ reduction. *Appl. Catal. B-Environ.* **226**, 463–472 (2018).
- Ju, W. et al. Understanding activity and selectivity of metal-nitrogen-doped carbon catalysts for electrochemical reduction of CO₂. *Nat. Commun.* **8**, 944 (2017).
- Zhang, H. et al. The synthesis of atomic Fe embedded in bamboo-CNTs grown on graphene as a superior CO₂ electrocatalyst. *Green Chem.* **20**, 3521–3529 (2018).
- Kang, Y. et al. Selective breaking of hydrogen bonds of layered carbon nitride for visible light photocatalysis. *Adv. Mater.* **28**, 6471–6477 (2016).
- Li, J. et al. Atomically dispersed manganese catalysts for oxygen reduction in proton-exchange membrane fuel cells. *Nat. Catal.* **1**, 935–945 (2018).
- Umezawa, Y. & Relley, C. N. Effect of argon ion bombardment on metal complexes and oxides studied by X-ray photoelectron spectroscopy. *Anal. Chem.* **50**, 1290–1295 (1978).
- Guo, Z. et al. Single-atom Mn–N₄ site-catalyzed peroxone reaction for the efficient production of hydroxyl radicals in an acidic solution. *J. Am. Chem. Soc.* **141**, 12005–12010 (2019).
- Guan, J. et al. Water oxidation on a mononuclear manganese heterogeneous catalyst. *Nat. Catal.* **1**, 870–877 (2018).
- Zhang, X. et al. Highly selective and active CO₂ reduction electrocatalysts based on cobalt phthalocyanine/carbon nanotube hybrid structures. *Nat. Commun.* **8**, 14675 (2017).
- Lu, Q. et al. A selective and efficient electrocatalyst for carbon dioxide reduction. *Nat. Commun.* **5**, 3242 (2014).
- Pan, Y. et al. Design of single-atom Co–N₅ catalytic site: a robust electrocatalyst for CO₂ reduction with nearly 100% CO selectivity and remarkable stability. *J. Am. Chem. Soc.* **140**, 4218–4221 (2018).
- Gao, D. et al. Size-dependent electrocatalytic reduction of CO₂ over Pd nanoparticles. *J. Am. Chem. Soc.* **137**, 4288–4291 (2015).
- Zheng, Y. et al. Molecule-level g-C₃N₄ coordinated transition metals as a new class of electrocatalysts for oxygen electrode reactions. *J. Am. Chem. Soc.* **139**, 3336–3339 (2017).
- Li, X. et al. Exclusive Ni–N₄ sites realize near-unity CO selectivity for electrochemical CO₂ reduction. *J. Am. Chem. Soc.* **139**, 14889–14892 (2017).
- Alvarez-Guerra, M., Albo, J., Alvarez-Guerra, E. & Irabien, A. Ionic liquids in the electrochemical valorisation of CO₂. *Energy Environ. Sci.* **8**, 2574–2599 (2015).

27. Rosen, B. A. et al. Ionic liquid-mediated selective conversion of CO₂ to CO at low overpotentials. *Science* **334**, 643–644 (2011).
28. Asadi, M. et al. Nanostructured transition metal dichalcogenide electrocatalysts for CO₂ reduction in ionic liquid. *Science* **353**, 467–470 (2016).
29. Zhu, Q. et al. Electrochemical reduction of CO₂ to CO using graphene oxide/carbon nanotube electrode in ionic liquid/acetonitrile system. *Sci. China Chem.* **59**, 551–556 (2016).
30. Feng, J. et al. Morphology modulation-engineered flowerlike In₂S₃ via ionothermal method for efficient CO₂ electroreduction. *ChemCatChem* **12**, 926–931 (2020).
31. Yang, D. et al. Selective electroreduction of carbon dioxide to methanol on copper selenide nanocatalysts. *Nat. Commun.* **10**, 677 (2019).
32. Costentin, C., Passard, G. & Savéant, J.-M. Benchmarking of homogeneous electrocatalysts: overpotential, turnover frequency, limiting turnover number. *J. Am. Chem. Soc.* **137**, 5461–5467 (2015).
33. Gurkan, B. E. et al. Equimolar CO₂ absorption by anion-functionalized ionic liquids. *J. Am. Chem. Soc.* **132**, 2116–2117 (2010).
34. Rosen, B. A. et al. In situ spectroscopic examination of a low overpotential pathway for carbon dioxide conversion to carbon monoxide. *J. Phys. Chem. C* **116**, 15307–15312 (2012).
35. Fujita, E., Furenli, L. R. & Renner, M. W. Direct XANES evidence for charge transfer in Co–CO₂ complexes. *J. Am. Chem. Soc.* **119**, 4549–4550 (1997).
36. Yang, H. et al. Atomically dispersed Ni (I) as the active site for electrochemical CO₂ reduction. *Nat. Energy* **3**, 140–147 (2018).
37. Sakaki, S. Can carbon dioxide coordinate to a nickel(I) complex? An ab initio MO/SD-CI study. *J. Am. Chem. Soc.* **112**, 7813–7814 (1990).
38. Zhao, K. et al. Selective electroreduction of CO₂ to acetone by single copper atoms anchored on N-doped porous carbon. *Nat. Commun.* **11**, 2455 (2020).
39. Sun, X. et al. Aqueous CO₂ reduction with high efficiency using atomic Ir electrocatalysts. *Angew. Chem. Int. Ed.* **58**, 4669–4673 (2019).
40. Rehr, J. J. & Albers, R. C. Theoretical approaches to x-ray absorption fine structure. *Rev. Mod. Phys.* **72**, 621–654 (2000).
41. Koningsberger, D. & Prins, R. (eds) *X-ray Absorption: Principles, Applications, Techniques of EXAFS, SEXAFS, and XANES* (Wiley, New York, 1988).
42. Ravel, B. & Newville, M. ATHENA, ARTEMIS, HEPHAESTUS: data analysis for X-ray absorption spectroscopy using IFEFFIT. *J. Synchrotron Radiat.* **12**, 537–541 (2005).
43. Kresse, G. & Furthmüller, J. Efficient iterative schemes for ab initio total-energy calculations using a plane-wave basis set. *Phys. Rev. B* **54**, 11169–11186 (1996).
44. Blochl, P. E. Projector augmented-wave method. *Phys. Rev. B* **50**, 17953–17979 (1994).
45. Perdew, J. P., Burke, K. & Ernzerhof, M. Generalized gradient approximation made simple. *Phys. Rev. Lett.* **77**, 3865–3868 (1996).
46. Nørskov, J. K. et al. Origin of the overpotential for oxygen reduction at a fuel-cell cathode. *J. Phys. Chem. B* **108**, 17886–17892 (2004).
47. Chen, Z., Mou, K., Yao, S. & Liu, L. Zinc-coordinated nitrogen-codoped graphene as an efficient catalyst for selective electrochemical reduction of CO₂ to CO. *ChemSusChem* **11**, 2944–2952 (2018).
48. Zhu, W. et al. Active and selective conversion of CO₂ to CO on ultrathin Au nanowires. *J. Am. Chem. Soc.* **136**, 16132–16135 (2014).
49. Pan, F. et al. Unveiling active sites of CO₂ reduction on nitrogen-coordinated and atomically dispersed iron and cobalt catalysts. *ACS Catal.* **8**, 3116–3122 (2018).
50. Zhu, M. et al. Covalently grafting cobalt porphyrin onto carbon nanotubes for efficient CO₂ electroreduction. *Angew. Chem. Int. Ed.* **58**, 6595–6599 (2019).
51. Zhao, C. et al. Ionic exchange of metal-organic frameworks to access single nickel sites for efficient electroreduction of CO₂. *J. Am. Chem. Soc.* **139**, 8078–8081 (2017).

Acknowledgements

This work is financially supported by the National Key R&D Program of China (2018YFB0605802), the National Natural Science Foundation of China (21838010, 21890762, 21921005), the DNL Cooperation Fund, CAS (DNL 180406), the Key Research Program of Chinese Academy of Science (ZDRW-ZS-2018-1-3), the Program of Beijing Municipal Natural Science Foundation (2182072, 2182071), and the International Partnership Program of Chinese Academy of Sciences (122111KYSB20190029). Thanks for the help of 1W1B station for XAFS testing.

Author contributions

J.Q.F. and H.S.G. performed the whole experiments. Z.P.C., S.J. Zeng and C.Y.J. worked on material characterizations. H.F.D. worked on electrocatalysis experiment. L.R.Z. worked on XAFS experiment. H.F.D., L.C.L., and S.J. Zhang analyzed the data. J.Q.F. and X.P.Z. co-wrote the paper. X.P.Z. conceived the project.

Competing interests

The authors declare no competing interests.

Additional information

Supplementary information is available for this paper at <https://doi.org/10.1038/s41467-020-18143-y>.

Correspondence and requests for materials should be addressed to S.Z. or X.Z.

Peer review information *Nature Communications* thanks the anonymous reviewers for their contribution to the peer review of this work.

Reprints and permission information is available at <http://www.nature.com/reprints>

Publisher's note Springer Nature remains neutral with regard to jurisdictional claims in published maps and institutional affiliations.



Open Access This article is licensed under a Creative Commons Attribution 4.0 International License, which permits use, sharing, adaptation, distribution and reproduction in any medium or format, as long as you give appropriate credit to the original author(s) and the source, provide a link to the Creative Commons license, and indicate if changes were made. The images or other third party material in this article are included in the article's Creative Commons license, unless indicated otherwise in a credit line to the material. If material is not included in the article's Creative Commons license and your intended use is not permitted by statutory regulation or exceeds the permitted use, you will need to obtain permission directly from the copyright holder. To view a copy of this license, visit <http://creativecommons.org/licenses/by/4.0/>.

© The Author(s) 2020